Thin-Plate Imaging Inspection Using Scattered Waves Cross-Correlation Algorithm and Non-Contact Air-Coupled Transducer

Wenfeng Xiao
Department of Mechanical Engineering,
University of South Carolina,
300 Main Street,
Columbia, SC 29208
e-mail: wxiao@email.sc.edu

Lingyu Yu[1]
Department of Mechanical Engineering,
University of South Carolina,
300 Main Street,
Columbia, SC 29208
e-mail: yu3@cec.sc.edu

This paper presents a non-contact air-coupled Lamb wave imaging technique using a two-dimensional (2D) cross-correlation method that not only detects the damage but also precisely quantifies for orientations and sizes. The air-coupled transducers (ACT) is used together with a scanning laser Doppler vibrometer (SLDV) for sensing, making a fully non-contact Lamb wave system used for this study. We first show that single-mode Lamb wave actuation can be achieved by the ACT-based on Snell's law. Detailed study and characterization of the directional ACT Lamb waves are conducted. For damage detection, a 2D cross-correlation imaging technique that uses the damage introduced scattered waves of all directions is proposed for correlating with the incident waves. The frequency-wavenumber filtering technique is used to implement the acquisition of the scated waves and incident waves, respectively. In the end application to notches with various orientations and various sizes in terms of depth and length is given. The results show the proposed technique can precisely imaging the damages and can quantitatively evaluate the damage size in terms of length and depth. [DOI: 10.1115/1.4048541]

Keywords: air-coupled transducer, single-mode Lamb waves, 2D cross-correlation imaging technique, evaluation of damage orientation and size, imaging, ultrasonics

1 Introduction

Lamb waves have been shown useful for damage detection in structural health monitoring (SHM) and nondestructive evaluation (NDE) in plate-like structures due to their ability to propagate long distances with less energy loss and sensitivity to small defects in the structure [1,2]. Although recent advances in Lamb wave-based SHM/NDE have demonstrated its feasibility of detecting and locating damage, there remain challenging issues due to the complexity involved with propagating Lamb waves. There are at least two Lamb wave modes, fundamental antisymmetric A_0 and symmetric S_0 modes, existing simultaneously where the product of the wave frequency f and structure half-thickness d falls in the range of 0–1 MHz mm [3]. When the product goes higher, even more wave modes (such as A_0, A_1, S_0, and S_1) can also be present. These wave modes will travel at different velocities depending on the frequencies, known as the dispersion phenomenon [4,5].

Lamb wave excitation and sensing are critical for damage detection in SHM/NDE. They can be generated and collected by a variety of means. Based on their installation requirements, Lamb wave transducers can be divided into two categories: contact type that needs to use liquid or solid couplant (e.g., piezoelectric wafer active sensors [6,7]; angle beam transducers [8]) and non-contact type that physical contact is not required. Contact transducers provide high energy actuation with high actuation efficiency. However, the additional bonding materials may contaminate the host structure or introduce uncontrollable issues, such as transduction mechanism and bonding layer degradation, which eventually will influence the effectiveness of the contact transducers [9]. Therefore, the non-contact method has attracted many interests in recent years. Several non-contact Lamb wave excitation methods including pulsed laser (PL) [10,11], air-coupled transducer (ACT)

[12–14], electromagnetic acoustic transducer (EMAT) [15], as well as sensing method using laser Doppler vibrometer [12] or laser vibrometry [16] have been reported. Among available non-contact transducers, piezoelectric air-coupled transducers (ACT) have emerged as a promising method [9]. Piezoelectric ACT works on the piezoelectric principle and uses air as the couplant to transduce the waves into solids. With a certain stand-off distance to the structure surface, the ACT is a truly non-intrusive method that eliminates the need for liquid couplant [17]. It actuates or senses Lamb waves based on Snell's law and can be controlled to achieve single-mode excitation or sensing [18]. Liu et al. [19] conducted ACT generation and reception of pure A_0 mode for single-side inspection of the delamination defects in composite materials. Harb and Yuan [20] investigated pure A_0 mode inspection of the barely visible impact damage using ACT for Lamb wave actuation.

One limitation with ACT Lamb wave SHM/NDE is the high attenuation of ultrasound in air and the energy loss at the air-structure interface caused by their impedance mismatch [14]. If ACT is used for both actuation and sensing, the loss could be significant and affect the application efficiency [18]. One solution is to replace either the actuation or sensing with a different type. Among various options, scanning laser Doppler vibrometer (SLDV) has emerged as a powerful means for non-contact remote sensing in ultrasonic wavefield measurement since it can make accurate surface velocity or displacement measurements over a spatially dense grid and provide high-resolution imaging sequences of wave propagation [21]. Staszewski et al. [22] illustrated the concept of Lamb wave propagation in the aluminum plate using a laser Doppler vibrometer and they also validated the results using classic piezoceramic-based sensing and numerical simulation. Kohler and Blackshire [23] studied the Lamb wave propagation in plate structures where sound wavefields were visualized as intensity and snapshot using a laser vibrometer.

Data analysis and damage evaluation techniques are of primary importance in applying any Lamb wave-based SHM/NDE [2]. Numerous approaches have been reported in the literature such as imaging-based ones including piezoelectric phased array

---

technique [24], time-migration-based imaging technique [25], frequency-wavenumber filtering method [26], and wavenumber analysis approach [27]. In the past few years, the cross-correlation imaging method has been introduced as one of the imaging detection method using the back-scattered waves and incident waves. Zhu et al. [28] developed a fast-real-time imaging method of multiple damage sites by cross-correlating the back-scattered waves and incident waves in the frequency domain. He and Yuan et al. [29] developed a zero-lag cross-correlation (ZLCC) imaging technique, using forward waves and the back-scattered waves to image structural damage in composites quantitatively. This ZLCC method utilizes all the input frequencies, and the dispersion effect was compensated automatically. Later, an enhanced imaging condition for composite damage imaging was developed which can provide enhanced imaging for multi-site damage as compared to the ZLCC method [30]. These reported imaging methods mostly cross-the incident waves with back-scattered waves generated at the damage. Yet indeed, when propagating Lamb waves encounter damage, it assembles a new wave source and generates scattered waves in all directions including back-scattered [31].

In this article, a fully non-contact Lamb wave system is established by judiciously combining the air-coupled transducer for actuation and scanning laser Doppler vibrometer for sensing. To reduce the complexity of the Lamb wave propagation, a single-mode Lamb wave inspection is achieved by controlling the ACT incident angle based on the Snell's law. A detailed characterization study is conducted to understand the ACT actuated Lamb wave. An advanced imaging technique based on the cross-correlation principle is developed for damage detection by innovatively using the damage scattered waves and the incident waves. The proposed imaging method is then applied to detect notches on steel plates. Two cases of notches with various orientations and sizes are studied to demonstrate how the present methods can evaluate defects in terms of orientations and sizes (length and depth). The paper is organized into five sections including this one (Sec. 1). Section 2 presents the configuration of a fully non-contact ACT-SLDV single-mode Lamb wave system with a detailed ACT Lamb wave propagation characterization study. Section 3 introduces the scattered waves cross-correlation imaging algorithm, followed with Sec. 4 the application on thin-plates with notches of various orientations and sizes. In the end, Sec. 5 summarizes the findings in the paper and outlines areas envisioned for future work.

2 Air-Coupled Transducers Lamb Wave Excitation

2.1 Single-Mode Air-Coupled Transducers Lamb Wave Excitation. Lamb waves are the guided waves that propagate in plate-like structures with stress-free surfaces. By solving the Rayleigh-Lamb wave equations numerically, the dispersion curves of the Lamb wave phase velocities can be obtained [3].

An example of the solved phase velocity dispersion curves of a 0.5 mm thick steel plate is shown in Fig. 1(a). In the given frequency range from 0 to 1000 kHz, there are only two fundamental Lamb wave modes, A_0 and S_0. A_0 mode phase velocity is smaller and more sensitive to the frequency change.

When ultrasonic waves travel through the air and hit an interface between air and plate with an incident angle θ (angle w.r.t. the plate plane normal direction), both reflected and refracted waves are produced [24]. Reflected waves are reflected in the air while refracted waves are transmitted into the plate and continue to propagate in the plate. After multiple reflections and accompanying mode conversion, Lamb waves are excited [9]. The excited Lamb wave mode is dependent on the incident angle θ and based on the Snell's law as [32],

$$\theta = \arcsin(c_{air}/c_{ph}) \tag{1}$$

where c_{ph} is the phase velocity of the Lamb wave and c_{air} is the sound speed in air. Using the Eq. (1), the dispersion curve of ACT Lamb waves in terms of the incident angle θ is further obtained from the phase velocity dispersion curve, as given in Fig. 1(b). It is seen that the ACT actuated A_0 Lamb wave is very sensitive to incident angle θ in the 0 to 1000 kHz frequency range, while S_0 mode incident angle θ remains constant at 5 deg or so. At any given frequency, the incident angles θ of A_0 and S_0 modes are discernible with that of A_0 mode always being larger. This manifests that a single-mode Lamb wave can be actuated by judiciously selecting the incident angle θ.

2.2 Non-Contact Single-Mode Lamb Wave Actuation and Sensing. In this study, single-mode A_0 Lamb wave actuation and sensing are performed. The ACT is a piezoelectric ceramic-based ACT transducer (AS400Ti) accompanied by the signal generation system (Airscan system, model #: SONDA-007CX). The ACT is a resonant type spherical point-focusing transducer with a nominal resonant frequency at 400 kHz and a focal length of about 25 mm. The incident angle θ determined from the dispersion curve (Fig. 1(b)) is experimentally calibrated and identified at 18 deg, which will be used in the subsequent experiments in this paper. On the sensing side, SLDV (model: Polytec PSV-400-M2) is used due to its advantage of rapid multi-dimensional wave propagation measurement with high spatial resolution [21].

The schematic setup of the ACT-SLDV system is given in Fig. 2(a). The Airscan system sends out a 5-count tone burst signal to the ACT for actuation, as well as a trigger signal to the SLDV system to initiate the data acquisition. The laser head of the SLDV system is placed normal to the plate surface for the out-of-plane velocity measurement of the wave propagation. To measure multidimensional wavefield, point grids at selected spatial resolution are defined. Reflective tape is placed on the test plate surface to improve the signal-to-noise ratio for SLDV
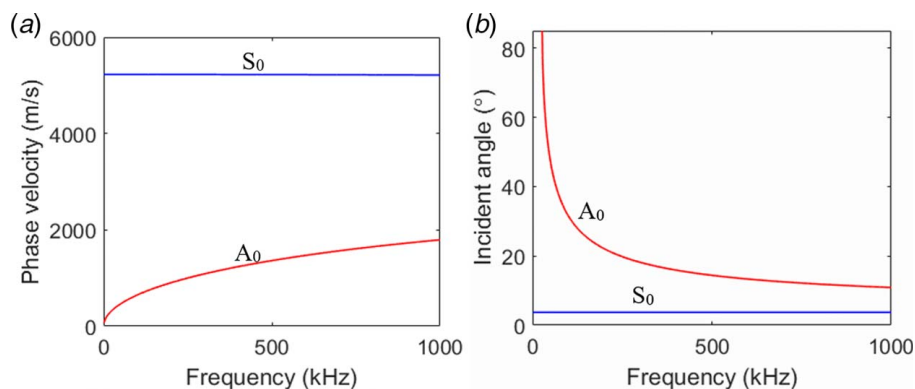
Fig. 1 Dispersion curves of 0.5 mm steel plate: (a) theoretical phase velocity dispersion curves and (b) incident angle dispersion curve obtained by the Snell's law
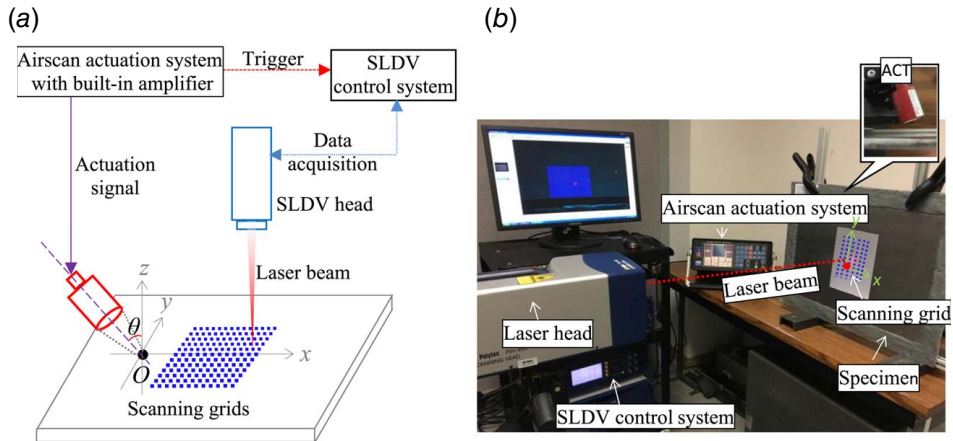
Fig. 2 The setups of the ACT-SLDV NDE system: (*a*) the overall schematic setup with the non-contact ACT actuation with incident angle *θ* and laser head placed normal to the plate to conduct the scan through the predefined scanning grids and (*b*) the laboratory experimental setup of the ACT-SLDV system

sensing. Details of SLDV wavefield sensing can be found in Ref. [21]. The laboratory experimental setup of the system is given in Fig. 2(*b*).

A preliminary ACT A_0 Lamb wave excitation has been conducted on a 0.5 mm thick stainless-steel T-304 plate. An *x*–*y*–*z* Cartesian coordinate system is defined with the ACT actuation point on the plate set as the origin *O* (Fig. 2(*a*)). A signal acquired at *x* = 20 mm is given in Fig. 3(*a*), showing a dominant first arrival about 54 μs spreading out in time domain. The corresponding frequency spectrum in Fig. 3(*b*) shows the signal has a center frequency around 370 kHz, which matches well with the nominal resonant frequency of the ACT. The full width at half maximum (FWHM) bandwidth is about 32 kHz, manifesting that the ACT provides a very narrow excitation and explains why the waveform

is quite spreading out in the time domain. Other than the dominant first arrival, it can be seen there is a very weak second arrival following behind. The cause could be a manufacturing deviation for backing or other which requires further detailed study in the future. In the current work, we are only focused on analyzing the first arrival for damage detection and evaluation according to Ref. [33].

The time-space wavefield is further acquired along the *x*-axis from 10 mm to 70 mm. At 370 kHz, the Lamb wave wavelength is about 3.2 mm. According to the sampling theorem [34], to sample the Lamb wave wavefield correctly, the spatial resolution should be at least or less than 1.6 mm. Moreover, higher spatial resolution will result in higher wavenumber resolution that can provide more accurate frequency-wavenumber information for
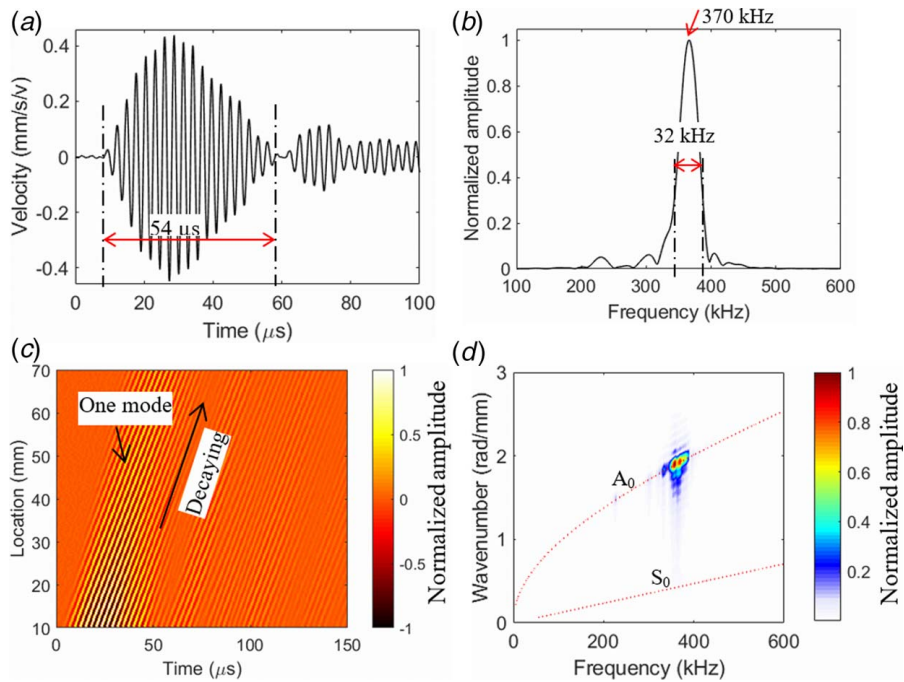
Fig. 3 ACT Lamb wave actuation results at 400 kHz: (*a*) waveform captured at *x* = 20 mm, (*b*) the frequency spectrum of the Lamb wave signal, showing narrow-band feature, and the resonant frequency at nearly excitation frequency (~370 kHz), (*c*) time-space wavefield within 10 to 70 mm propagation range, and (*d*) frequency-wavenumber spectrum showing the presence of dominant A0 mode

subsequent wavenumber processing. However, higher spatial resolution comes at a cost of longer data acquisition time. Therefore, considering a balance between wavenumber resolution and data acquisition time, a spatial resolution at 0.5 mm was used in our experiments. The measured wavefield is given in Fig. 3(c), and it shows that the wave attenuates as the wave propagates. To identify the Lamb wave mode actuated by the ACT, intrinsic time-frequency analysis given out in Ref. [26] is conducted. The transformed frequency-wavenumber spectrum is shown in Fig. 3(d), along with the theoretical frequency-wavenumber curves by solving the Rayleigh-Lamb wave equations numerically. By comparing the experimental values with the theoretical, it confirms that single-mode A_0 Lamb wave excitation and sensing is achieved.

2.3 Air-Coupled Transducers Lamb Wave Directionality Study. In this study, the ACT Lamb wave propagation has been observed to be highly directional, as illustrated in the two-dimensional (2D) Lamb wave propagation in Fig. 4(a) and being consistent with what's reported in the literature [35]. Most of the waves are along the $+x$-direction which aligns with the ACT transducer centerline. To properly use the ACT Lamb wave for optimal damage detection, directionality analysis needs to be conducted. The setups for directionality study are given in Fig. 4(a), with the α being the angular position (w.r.t. $+x$-axis for wave propagation direction, -180 deg to 180 deg) and R being the radial distance for wave propagation (w.r.t. the coordinate Origin) for parametric study.

The waves at different directions α after propagating the same distance are first studied. Figure 4(b) shows selected waves at -10 deg, 0 deg, and 10 deg at $R = 40$ mm. Indicated by the peak-to-peak value of the dominant wave package, the signal at 0 deg (i.e., along with the ACT centerline and $+x$-direction) is noted much stronger when compared with signals at ±10 deg. Furthermore, signals of all directions from -180 deg to 180 deg are collected at 1 deg resolution with different propagation distances at $R = 20$, 40, 60 mm. The normalized peak-to-peak values are then determined and plotted w.r.t. the direction α in Fig. 4(c).

The plot confirms that the ACT Lamb wave is highly directional with its strongest propagation along 0 deg direction where the ACT centerline is in, and then rapidly decreasing and resulting in a very narrow intensity beam within about ±40 deg. The directionality at different propagation distances R has also been studied. As seen in Fig. 4(c), similar directionality at all propagating distances are obtained. In a certain direction, such as 0 deg, the intensity decreases as the propagating distance increases from 20 mm to 60 mm. This indicates as the propagation distance increases, the intensity of the waves decreases.

To better examine the wave strength at other directions, the intensities within ±40 deg directions are further plotted in Fig. 4(d). The waves at different distances all have their peak intensities along $\alpha = 0$ deg. Besides, by adding a 36% threshold, it is found the wave propagation is mostly focused in the ±18 deg range. Beyond that range, the wave propagation decreased significantly. The directionality result demonstrates that the ACT Lamb wave is directional with its strongest intensity along the ACT centerline direction.

3 Cross-Correlation Imaging Using Scattered Waves

3.1 Overview of the Cross-Correlation Imaging. The cross-correlation imaging technique was first introduced in the context of reverse time migration by Chang and McMechan [36]. Conventionally cross-correlation imaging can be implemented in either the time (t) or frequency domain (f) using a source wavefield (Ws) and a receiver wavefield (Wr) [37]. The imaging condition is defined based on the concept that if both source waves and the receiver waves are extracted separately, these two wavefields kinematically coincident at the discontinuities, and the magnitude of cross-correlation values at the discontinuities will be much larger than that of the remaining locations where it will be small or near zero. The cross-correlation imaging method for damage detection is originally proposed by Zhu et al. [28] for multiple damage identification in the aluminum plate using the incident waves and back-scattered waves by a permanently mounted linear array of
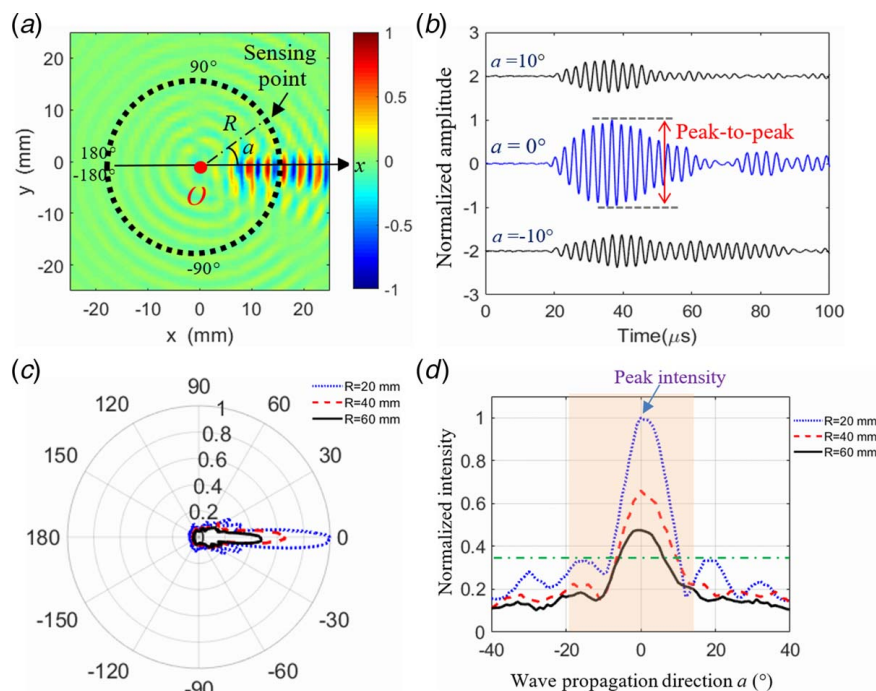
Fig. 4 Directionality study of the 2D ACT Lamb wave propagation: (a) 2D ACT Lamb wave wavefield at 28 μs, (b) the waveforms of α = 0 deg and α = ±10 deg directions with the same propagation distance, (c) the directionality results of all directions with propagation distance of 20 mm, 40 mm, and 60 mm, and (d) the detailed directionality result within ±40 deg

piezoelectric wafers. He and Yuan [29] later investigated cross-correlation imaging for damage inspection in composite structures using flexural wave signals. Most of the reported cross-correlation imaging work used the incident waves (source wave) with the back-scattered waves (receiver wave) for the damage detection. However, when incident waves interact with damage or defect, scattered waves in all directions are indeed generated as reported in the literature [28]. As compared to the back-scattered waves, these scattered waves in all directions may contain more information regarding the overall information of the damage toward its quantification.

3.2 Scattered Wave Cross-Correlation Imaging. In this study, a 2D cross-correlation imaging method in the time domain that uses scattered waves of all directions as the receiver wave and incident waves as the source wave is proposed for precisely damage imaging. The imaging algorithm is expressed as

$$X_{\text{corr}}(\mathbf{x}) = \int_0^T v_{\text{incident}}(\mathbf{x}, t) v_{\text{scattered}}(\mathbf{x}, t) dt \qquad (2)$$

where $v_{\text{incident}}(\mathbf{x}, t)$ is the incident wave wavefield, $v_{\text{scattered}}(\mathbf{x}, t)$ is the damage scattered wave wavefield, and $X_{\text{corr}}(\mathbf{x})$ is the cross-correlation value at $\mathbf{x}$.

To separate the incident waves and scattered waves for cross-correlation imaging, the frequency-wavenumber filtering method [26] is used. The process is briefly introduced here for the completeness of knowledge. The first step is to transfer the time-space wavefield to the frequency-4wavenumber domain using the Fourier transform method. For 2D wavefield $v(t, x)$, it is given as

$$V(f, \mathbf{k}) = \int_{-\infty}^{\infty} \int_{-\infty}^{\infty} v(t, \mathbf{x}) e^{-j(2\pi ft - \mathbf{k} \cdot \mathbf{x}) dt d\mathbf{x}} \qquad (3)$$

where $V(f, \mathbf{k})$ is the resulted frequency-wavenumber representation in terms of the frequency f and the wavenumber vector $\mathbf{k}$ which is defined as (k_x, k_y). Within the frequency-wavenumber domain, a wavenumber filter $V(f, \mathbf{k})$ (similar to digital filter used in the frequency domain [21]) is designed to filter the incident wave and scattered wave wavenumbers. The filtering process is mathematically expressed as the product between the waves' frequency-wavenumber representation $V(f, \mathbf{k})$ and the designed frequency-wavenumber filter $F(f, \mathbf{k})$ as follows:

$$V_F(f, \mathbf{k}) = V(f, \mathbf{k}) F(f, \mathbf{k}) \qquad (4)$$

where $V_F(f, \mathbf{k})$ represents the resulted filtered spectrum.

Lamb wave propagation in terms of frequency-wavenumber characterization in a structure depends on the frequency and plate thickness [5]. During wave propagation, when damage happens, it will modify the wave propagation in many ways by its size and orientation. These modifications may introduce scattered waves that propagate with new wavenumbers [31]. An example of wavenumber representatives of ACT Lamb waves in a pristine plate and a plate with a notch is given in Fig. 5 plotted with the circles represent the theoretical wavenumbers. In Fig. 5(a), only wavenumbers along with the positive theoretical wavenumber present, which represent the incident waves. In Fig. 5(b), some new higher wavenumbers other than the incident wavenumber are observed. From the comparison of the wavenumber spectrum, strong new higher wavenumbers due to the notch are observed, and they are treated as related to the notches scattered waves.

To filter the incident waves, a bandpass filter $F_{in}(f, \mathbf{k})$ is designed to retain incident wave wavenumbers. Since ACT Lamb waves are highly directional and mainly focus on the positive x-direction, only positive k_x will be retained. An example of the filter at 370 kHz is given in Fig. 6(a) along with A_0 theoretical wavenumber. The 1D zoom-in filter ($k_y = 0$; 1.5 rad/mm $\leq k_x \leq$ 2.5 rad/mm) demonstrates that only wavenumbers centered at the theoretical A_0 wavenumber are retained.

To filter the new higher wavenumbers of the scattered waves, a highpass filter is designed. Besides, the scattered waves may
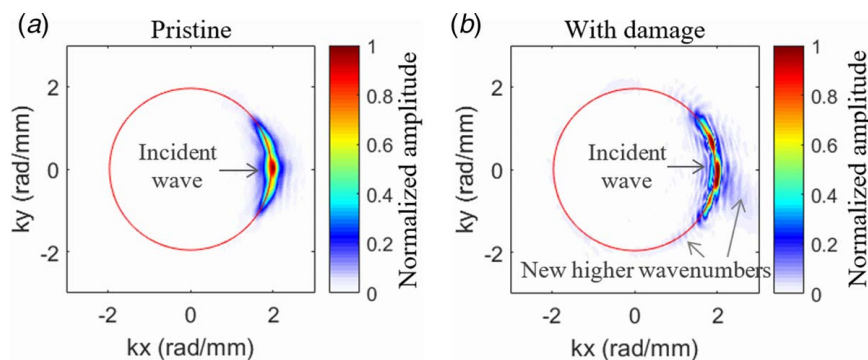
Fig. 5 Lamb wave wavenumber comparison of pristine plate and plate with a notch at 370 kHz. Wavenumbers of (a) pristine plate and (b) plate with notch damage.
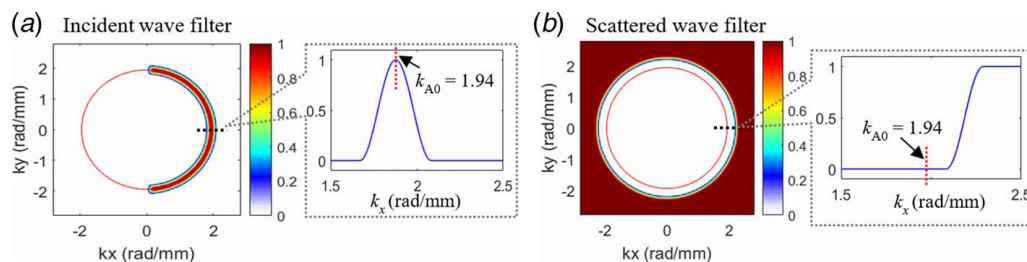
Fig. 6 Wavenumber filters for the incident waves and scattered waves at 370 kHz. (a) The band-pass filter for the incident waves of positive kx where only wavenumber band centered at the theoretical A0 wavenumber kA0 is retained. (b) The high-pass filter for the scattered waves where wavenumbers larger than kA0 of all directions are retained.
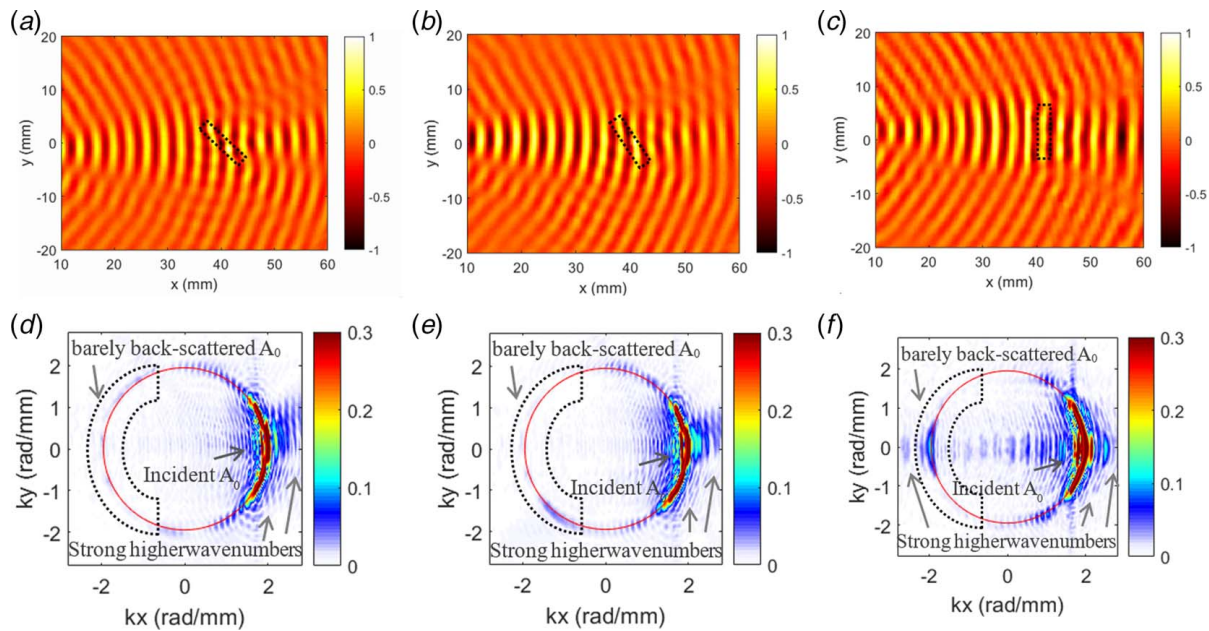
Fig. 7 The wavefields acquired by the SLDV at 40 μs in 0.5 mm steel plate with half-thickness notches of (*a*) 45 deg orientation, (*b*) 60 deg orientation, and (*c*) 90 deg orientation. Panels (*d*), (*e*), and (*f*) are wavenumber spectra at 370 kHz by three-dimensional Fourier transformation (3DFT) method for 45 deg, 60 deg, and 90 deg notches, respectively.

propagate in any random direction due to the uncertainty of the damage. Therefore, the highpass filter is designed along with all directions. An example of the filter at 370 kHz is given in Fig. 6(*b*) along with the theoretical wavenumber of A_0 Lamb wave. The one-dimensional (1D) zoom-in filter ($k_y = 0$; 1.5 rad/mm $\leq k_x \leq 2.5$ rad/mm) demonstrates that only wavenumber components higher than theoretical wavenumber of A_0 ($k_A = 1.94$ rad/mm) are retained. The filtered incident wave wavefield $v_{incident}$ (**x**, *t*) and scattered wave wavefield $v_{scattered}$ (**x**, *t*) can be further obtained for cross-correlation imaging by converting from the filtered wavenumber spectra using the inverse 3DFT method.

4 Damage Imaging and Evaluation

The improved cross-correlation imaging technique is applied to detect notches of various orientations (Case 1) or sizes (Case 2) on steel plates using the ACT-SLDV non-contact Lamb wave system.

4.1 Case 1: Notches With Various Orientations. Three 0.5 mm thick T304 steel plate samples with a half-thickness notch (length × width × depth: 10 mm × 2 mm × 0.25 mm) of 45 deg, 60 deg, and 90 deg orientations are prepared. The notches are centered at x = 40 mm (Fig. 2). With Lamb waves actuated at the Origin by the ACT, 2D time-space wavefields are acquired with a 0.5 mm spatial resolution. The wavefields of three situations at 40 μs are given in Figs. 7(*a*)–7(*c*), respectively. Wave-damage interactions are observed at the notch locations in the three wavefields. All wavefields in the study are normalized by their own maximum amplitude individually to show the wave propagation or interactions at the damage. However, from the wavefield information, it is difficult to quantify the notch defects, neither to tell their differences in orientations. The 2D cross-correlation imaging algorithm outlined in Sec. 3 is then implemented for further notch evaluation.

The frequency-wavenumber spectra of the three situations are first obtained by converting from the time-space wavefield using the 3DFT method. The wavenumber spectra at 370 kHz frequency for all plates are shown in Figs. 7(*d*)–7(*f*), respectively, with the circles in red represent the theoretical wavenumber of A_0 mode. Strong incident A_0 wavenumbers are found in all plates. Besides,

dominant higher wavenumbers that introduced by the notches all are observed in different plates. Other than that, barely visible wavenumbers of back-scattered waves are seen. Applying the frequency-wavenumber filtering method with the incident wave bandpass filter and scattered wave highpass filter as proposed in Sec. 3.2, the corresponding wavenumbers are then filtered. Representative scattered wave wavenumber spectra at 370 kHz are given in Figs. 8(*a*)–8(*c*), respectively, plotted along with the theoretical A_0 wavenumbers. It is noted that new higher wavenumbers of all directions are achieved in the plates, demonstrating scattered waves of all directions are successfully filtered. Using the inverse 3DFT method, the incident wave and scattered wave wavefields are then obtained. The all-directional scattered waves provided overall dimensions of the damage and could significantly improve the accuracy of the cross-correlation imaging.

The imaging method outlined in Sec. 3 was now applied, as well as the ZLCC algorithm using the primary reflective waves [29] for comparison. The results are presented in Fig. 9, respectively. Figure 9(*a*) from ZLCC and Fig. 9(*b*) from our method show the latter significantly improved the imaging resolution and gave a precise mapping of the notch damage with correct indication of the notch orientation in the plate. The possible reason is that the ZLCC method uses the back-scattered waves which are very weak as shown in the wavenumber components presentation in Fig. 7(*a*) due to the small size of the damage in this study. However, there are much stronger forward scattered waves (i.e., the higher positive wavenumbers) as shown in Fig. 7(*a*).

The proposed cross-correlation algorithm was further applied to the 60 deg, and 90 deg orientation notches and the imaging results are given in Figs. 10(*a*) and 10(*b*), respectively, plotted along with the realistic notches. From comparisons of the notch image with the realistic notches, both notches are precisely imaged with their orientations and locations match very well. The capability of the proposed cross-correlation imaging technique for precisely damage imaging with various orientations has been demonstrated successfully.

4.2 Case 2: Inspection of Damages With Various Sizes. To investigate the proposed imaging technique for damages with variable sizes, three 0.5 mm thick T304 steel plate samples with notches of various sizes are machined. In this case, the notch with a
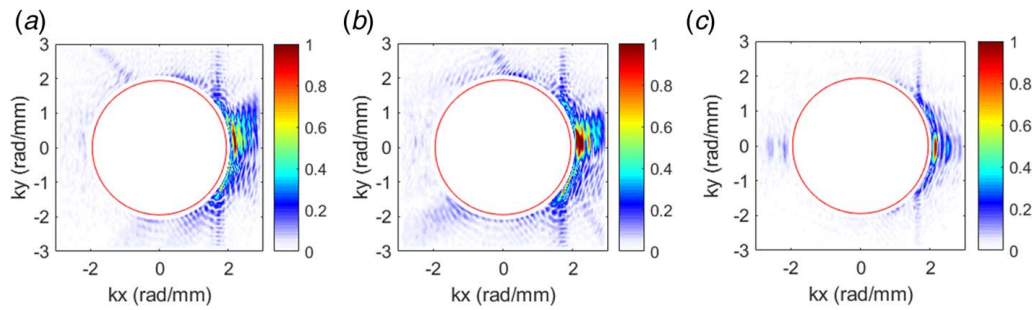
Fig. 8 Filtered all-directional scattered wave wavenumbers in plates with half-thickness notches of (a) 45 deg, (b) 60 deg, and (c) 90 deg orientations. The spectra show that scattered wave wavenumbers of all directions are successfully achieved.
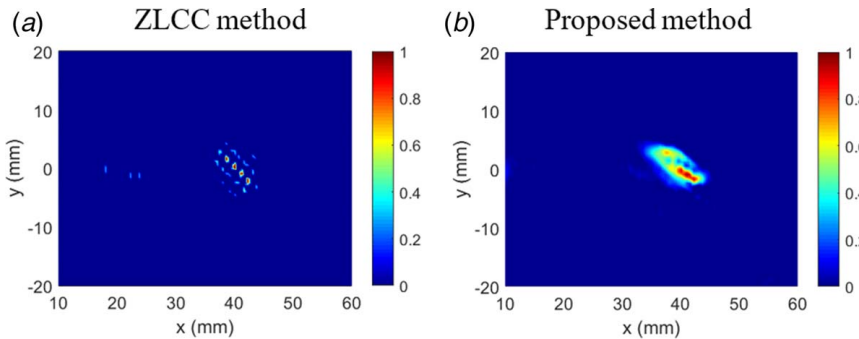
Fig. 9 Cross-correlation imaging comparison of 45 deg notch: (a) the ZLCC method uses the back-scattered waves and (b) the newly proposed method uses the scattered waves of all directions
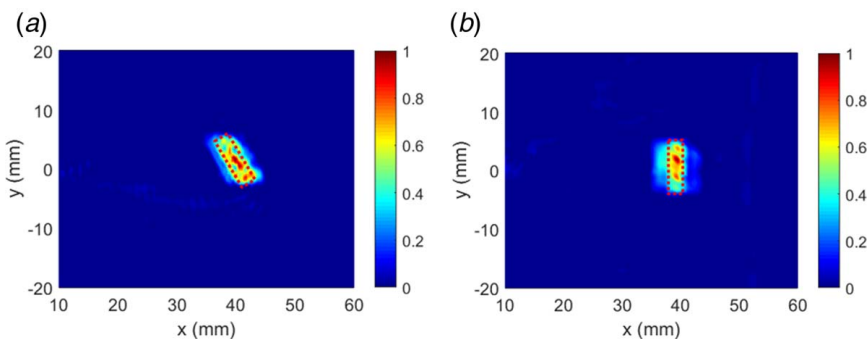

Fig. 10 The proposed cross-correlation imaging for half-thickness notches of (a) 60 deg and (b) 90 deg orientation

dimension of 10 mm × 2 mm × 0.25 mm (length × width × depth) is set as reference notch; a shallower notch with 0.1 mm depth is set as the shallow notch for depth detection and evaluation, and a shorter notch with 3 mm length is set as the short notch for length detection and evaluation. All notches are aligned at $x = 40$ mm for inspection.

With SLDV 2D scanning, the wavefields of these three notches are acquired and wavefields at the selected time of $40\,\mu s$ are given in Figs. 11(a)–11(c), respectively. Wave-damage interactions all are observed in the three plates. The reference notch provides the strongest wave interactions as compared to those of shallow notch and short notch since it has the largest dimension in both length and depth. However, from the wavefields, it is difficult to quantify and evaluate the notch sizes. By implementing the proposed cross-correlation imaging technique in Sec. 3.2, all notches are successfully imaged as given in Figs. 11(d)–11(f). For comparison and quantification purposes, the cross-correlation values I of

three situations are normalized by the peak value of the reference notch. As plotted along with the realistic notch locations and dimensions, it can be found all notches are precisely imaged with locations and notch shapes match very well. For the notch depth detection, it is noted that the peak X_{corr} of the shallow notch is in pale yellow (around 0.5 in the color bar) while the peak X_{corr} of reference notch is in red (around 1 in the color bar). This difference indicates that the imaging method is capable to discern the notches of different depths. For the notch length detection, the imaging result of the short notch is significantly shorter as compared to that of the reference notch, demonstrating the notches of different length successfully identified. Moreover, the peak X_{corr} of the short notch and reference notch all are in red color since they have the same depth, which further validates the proposed imaging method is feasible for notch depth detection.

To quantitatively evaluate the notch depth, the X_{corr} of the shallow notch, and the reference notch along the x-axis line are
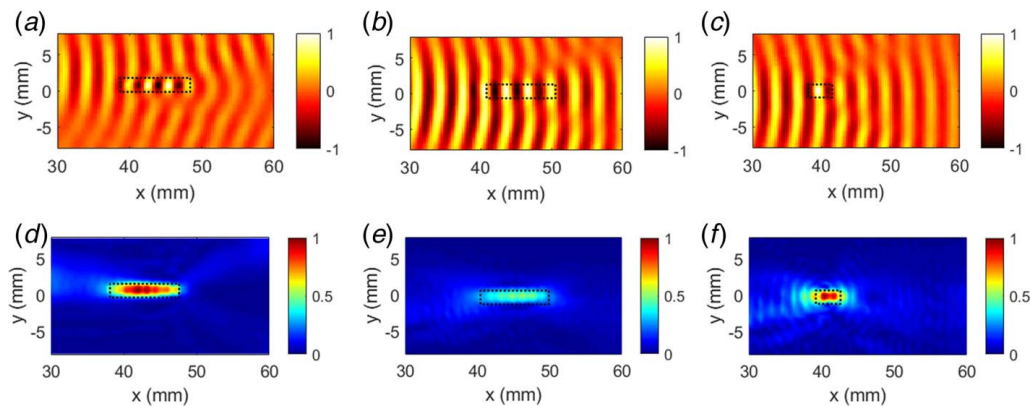
Fig. 11 The imaging inspection of notches with various sizes in depth and length. The SLDV acquired time-space wavefields of (a) reference notch, (b) shallow notch, and (c) short notch at 40 μs. The cross-correlation imaging results of (d) reference notch, (e) shallow notch, and (f) short notch. Note, the $I(x, y)$ value of them is normalized by the reference notch for comparison.
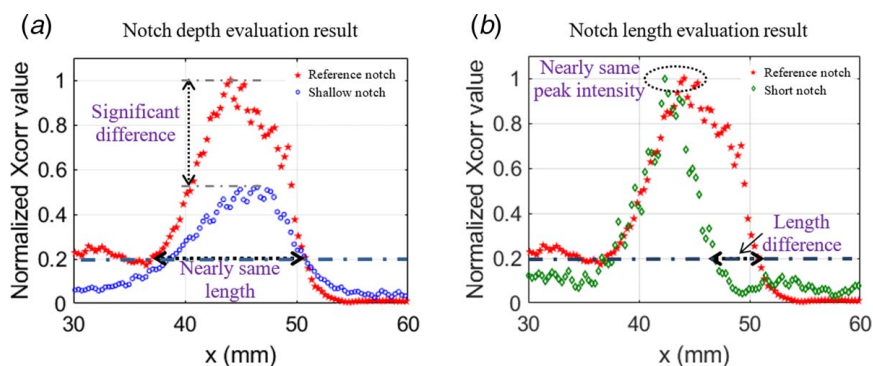
Fig. 12 The evaluations of the notches with different sizes by the cross-correlation method. (a) The cross-correlation evaluation of the 10 mm notches with different depth of 0.25 mm and 0.1 mm. The peak X_{corr} value is significantly decreased when the notch is shallower. (b) The cross-correlation evaluation of the same depth notch but the different length of 10 mm and 3 mm. The significant length difference is observed. And same peak X_{corr} values are observed since they have the same depth.

plotted together as shown in Fig. 12(a) for further analysis. It is found that the peak X_{corr} value of the reference notch with 0.25 mm depth is 1, while the peak X_{corr} of the shallow notch with 0.1 mm depth is significantly decreased to about 0.5. This indicates the 0.15 mm difference in depth is successfully identified, demonstrating that the cross-correlation method can quantitatively evaluate the notch depth. Furthermore, by adding a threshold at 0.2, both the reference notch and the shallow notch are identified nearly the same which is consistent with the realistic same length of these two notches.

Similarly, to quantitatively evaluate the notch length, the X_{corr} of the short notch and the reference notch along the x-axis line are plotted together as given in Fig. 12(b) for analysis. Nearly the same peak values of these two notches are observed which is consistent with the real condition and confirms that these two notches have the same depth. By adding the same threshold at 0.2, the lengths of the notches are observed to be different, indicating that the different notch lengths are quantitatively detected. The notch length and depth evaluation results demonstrating the quantification capability of the proposed imaging technique for notches of various sizes in depth and length.

5 Summary, Conclusions, and Future Work

This paper presents a 2D cross-correlation imaging method for damage detection using a completely non-contact ACT-SLDV system and single-mode Lamb waves. First, the non-contact system was configured using the ACT for Lamb wave actuation and SLDV for Lamb wave measurement. For the ACT Lamb wave actuation, a single-mode Lamb wave can be achieved by controlling the incident angle. To achieved single-mode Lamb waves by ACT, the incident angles were first theoretically obtained by transferring from the phase velocity dispersion curves based on Snell's law. With SLDV multi-dimensional wave propagation measurement, the ACT Lamb wave propagation was observed highly directional. Signal intensity change is a criterion for Lamb wave-damage detection; however, if the signal intensity change is induced by the directional wave propagation, it will lose the damage detection efficiency. To properly use the ACT Lamb wave for damage detection, directionality analysis of the 2D wave propagation was conducted. Next, a 2D cross-correlation imaging method for damage detection using incident waves and scattered waves was proposed. To capture more information about the overall dimension of the damage, the scattered waves of all directions were proposed for imaging implementation. The frequency-wavenumber filtering method was adopted to separate the incident waves and scattered waves. A bandpass filter with positive wavenumber k_x was proposed to filter incident waves only, and a highpass filter of all directions was proposed to filter the scattered waves of all directions. Thus, the damage overall dimension could be retained. Finally, the proposed imaging technique was implemented for inspections of notches with various orientations and various sizes in a 0.5 mm thick stainless-steel T 304 plate.

The single-mode Lamb waves actuation and sensing result show that single-mode A_0 Lamb wave was successfully achieved by controlling the ACT incident angle based on the Snell's law. In addition, it was found that the ACT was a narrowband excitation and its FWHM bandwidth was about 32 kHz. The ACT Lamb wave directionality study showed that the strongest Lamb wave propagated along the ACT centerline (x-axis) and wave propagation mostly focused in the ±18 deg range about the ACT center. Beyond that, the wave propagation decreased significantly. The imaging results of the notches with various orientations (45 deg, 60 deg, and 90 deg) match well with the realistic notch orientations, demonstrating the capability of the proposed imaging algorithm for precisely notch detection. Furthermore, the quantification results of the notches with various sizes (different lengths of 3 mm and 10 mm; different depths of 0.1 mm and 0.25 mm) show that the proposed algorithm can quantify the notch depth as shallow as 0.1 mm and notch length as small as 3 mm. The feasibility of the proposed imaging technique for both notch orientations and sizes evaluations has been successfully demonstrated.

For future work, more complicated damage scenarios should be investigated towards the application of engineer structures, such as the fatigue cracks and corrosion damages. Moreover, the proposed method should be extended to the inspection of composite structures. Additional work on investigating the second weaker wave packet from the ACT transducer shall also be conducted.

Acknowledgment

Data Availability Statement

The datasets generated and supporting the findings of this article are obtainable from the corresponding author upon reasonable request. The authors attest that all data for this study are included in the paper.

References

[1] Rose, J. L., 2014, *Ultrasonic Guided Waves in Solid Media*, Cambridge University Press, New York.

[2] Yuan, F., 2016, *Structural Health Monitoring (SHM) in Aerospace Structures*, Woodhead Publihsing, Cambridge, UK.

[3] Giurgiutiu, V., 2007, *Structural Health Monitoring: with Piezoelectric Wafer Active Sensors*, Elsevier, New York.

[4] Mei, H., and Giurgiutiu, V., 2019, "Guided Wave Excitation and Propagation in Damped Composite Plates," Struct. Health. Monit., 18(3), pp. 690–714.

[5] Su, Z., Ye, L., and Lu, Y., 2006, "Guided Lamb Waves for Identification of Damage in Composite Structures: A Review," J. Sound Vib., 295(3–5), pp. 753–780.

[6] Yu, L., and Giurgiutiu, V., 2008, "In Situ 2-D Piezoelectric Wafer Active Sensors Arrays for Guided Wave Damage Detection," Ultrasonics, 48(2), pp. 117–134.

[7] Mei, H., Haider, M. F., Joseph, R., Migot, A., and Giurgiutiu, V., 2019, "Recent Advances in Piezoelectric Wafer Active Sensors for Structural Health Monitoring Applications," Sensors, 19(2), p. 383.

[8] Mei, H., Haider, M. F., James, R., and Giurgiutiu, V., 2020, "Pure S0 and SH0 Detections of Various Damage Types in Aerospace Composites," Composites, Part B, 189, p. 107906.

[9] Liu, Z., Yu, H., He, C., and Wu, B., 2013, "Delamination Damage Detection of Laminated Composite Beams Using air-Coupled Ultrasonic Transducers," Sci. China: Phys., Mech. Astron., 56(7), pp. 1269–1279.

[10] An, Y. K., Park, B., and Sohn, H., 2013, "Complete Noncontact Laser Ultrasonic Imaging for Automated Crack Visualization in a Plate," Smart Mater. Struct., 22(2), p. 025022.

[11] Tian, Z., Howden, S., Ma, Z., Xiao, W., and Yu, L., 2019, "Pulsed Laser-Scanning Laser Doppler Vibrometer (PL-SLDV) Phased Arrays for Damage Detection in Aluminum Plates," Mech. Syst. Signal Process., 121, pp. 158–170.

[12] Harb, M. S., and Yuan, F. G., 2016, "Damage Imaging Using non-Contact Air-Coupled Transducer/Laser Doppler Vibrometer System," Struct. Health. Monit., 15(2), pp. 193–203.

[13] Harb, M. S., and Yuan, F. G., 2016, "Non-Contact Ultrasonic Technique for Lamb Wave Characterization in Composite Plates," Ultrasonics, 64, pp. 162–169.

[14] Xiao, W. F., and Lu, C., 2015, "Measuring the Disperse Curves of air-Coupled Lamb Waves in Glass Fibre Reinforced Aluminium Laminate Based on Time–Frequency Analysis," Mater. Res. Innovations, 19(sup9), pp. S9–106.

[15] Salzburger, H. J., Niese, F., and Dobmann, G., 2012, "EMAT Pipe Inspection with Guided Waves," Weld. World, 56(5–6), pp. 35–43.

[16] Leong, W. H., Staszewski, W. J., Lee, B. C., and Scarpa, F., 2005, "Structural Health Monitoring Using Scanning Laser Vibrometry: III. Lamb Waves for Fatigue Crack Detection," Smart Mater. Struct., 14(6), p. 1387.

[17] Yan, F., Hauck, E., Mor Pera, T., and Rose, J. L., 2007, "Ultrasonic Guided Wave Imaging of a Composite Plate with Air-Coupled Transducers," AIP Conference Proceedings, AIP, March, Vol. 894, No. 1, pp. 1007–1012.

[18] Harb, M. S., and Yuan, F. G., 2015, "A Rapid, Fully non-Contact, Hybrid System for Generating Lamb Wave Dispersion Curves," Ultrasonics, 61, pp. 62–70.

[19] Liu, Z., Yu, H., He, C., and Wu, B., 2014, "Delamination Detection in Composite Beams Using Pure Lamb Mode Generated by air-Coupled Ultrasonic Transducer," J. Intell. Mater. Syst. Struct., 25(5), pp. 541–550.

[20] Harb, M. S., and Yuan, F. G., 2017, "Barely Visible Impact Damage Imaging Using Non-Contact Air-Coupled Transducer/Laser Doppler Vibrometer System," Struct. Health. Monit., 16(6), pp. 663–673.

[21] Yu, L., and Tian, Z., 2013, "Lamb Wave Structural Health Monitoring Using a Hybrid PZT-Laser Vibrometer Approach," Struct. Health. Monit., 12(5–6), pp. 469–483.

[22] Staszewski, W. J., Lee, B. C., Mallet, L., and Scarpa, F., 2004, "Structural Health Monitoring Using Scanning Laser Vibrometry: I. Lamb Wave Sensing," Smart Mater. Struct., 13(2), p. 251.

[23] Köhler, B., and Blackshire, J. L., 2006, "Laser Vibrometric Study of Plate Waves for Structural Health Monitoring (SHM)," AIP Conference Proceedings, American Institute of Physics, March, Vol. 820, No. 1, pp. 1672–1679.

[24] Yu, L., and Leckey, C. A., 2013, "Lamb Wave–Based Quantitative Crack Detection Using a Focusing Array Algorithm," J. Intell. Mater. Syst. Struct., 24(9), pp. 1138–1152.

[25] Kannusamy, M., Kapuria, S., and Sasmal, S., 2020, "Accurate Baseline-Free Damage Localization in Plates Using Refined Lamb Wave Time-Reversal Method," Smart Mater. Struct., 29(055044), pp. 1–17.

[26] Ruzzene, M., 2007, "Frequency-wavenumber Domain Filtering for Improved Damage Visualization," Ultrasonic And Advanced Methods For Nondestructive Testing And Material Characterization, pp. 591–611.

[27] Rogge, M. D., and Leckey, C. A., 2013, "Characterization of Impact Damage in Composite Laminates Using Guided Wavefield Imaging and Local Wavenumber Domain Analysis," Ultrasonics, 53(7), pp. 1217–1226.

[28] Zhu, R., Huang, G. L., and Yuan, F. G., 2013, "Fast Damage Imaging Using the Time-Reversal Technique in the Frequency–Wavenumber Domain," Smart Mater. Struct., 22(7), p. 075028.

[29] He, J., and Yuan, F. G., 2015, "Damage Identification for Composite Structures Using a Cross-Correlation Reverse-Time Migration Technique," Struct. Health. Monit., 14(6), pp. 558–570.

[30] He, J., and Yuan, F. G., 2016, "A Quantitative Damage Imaging Technique Based on Enhanced CCRTM for Composite Plates Using 2D Scan," Smart Mater. Struct., 25(10), p. 105022.

[31] Chia, C. C., Lee, J. R., Park, C. Y., and Jeong, H. M., 2012, "Laser Ultrasonic Anomalous Wave Propagation Imaging Method With Adjacent Wave Subtraction: Application to Actual Damages in Composite Wing," Opt. Laser Technol., 44(2), pp. 428–440.

[32] Xiao, W., and Yu, L., 2019, "Nondestructive Evaluation with Fully non-Contact air-Coupled Transducer-Scanning Laser Doppler Vibrometer Lamb Wave System," Nondestructive Characterization and Monitoring of Advanced Materials, Aerospace, Civil Infrastructure, and Transportation XIII, International Society for Optics and Photonics, April, Vol. 10971, p. 109711G.

[33] Michaels, J. E., 2017, "Ultrasonic Wavefield Imaging: Research Tool or Emerging NDE Method?," AIP Conference Proceedings, AIP Publishing LLC, February, Vol. 1806, No. 1, p. 020001.

[34] Zayed, A., 2018, *Advances in Shannon's Sampling Theory*, Routledge, New York.

[35] Chennamsetti, R., and Khan, I., 2015, "A0 Lamb Mode Radiation Characteristics of air-Coupled Transducers in Isotropic Plates," Int. J. Precis. Eng. Manuf., 16(1), pp. 121–125.

[36] Chang, W. F., and McMechan, G. A., 1986, "Reverse-time Migration of Offset Vertical Seismic Profiling Data Using the Excitation-Time Imaging Condition," Geophysics, 51(1), pp. 67–84.

[37] Sava, P., and Vlad, I., 2011, "Wide-Azimuth Angle Gathers for Wave-Equation Migration," Geophysics, 76(3), pp. S131–S141.